Nanoscale Horizons

The home for rapid reports of exceptional significance in nanoscience and nanotechnology

rsc.li/nanoscale-horizons

ROYAL SOCIETY
OF **CHEMISTRY**

COMMUNICATION
Tie Yu, Weiqiao Deng *et al.*
Single-atom alloy Ir/Ni catalyst boosts CO_2 methanation *via* mechanochemistry

NCNST

Check for updates

Single-atom alloy Ir/Ni catalyst boosts CO_2 methanation *via* mechanochemistry†

Rui Tu,‡ Yujie Zhang,‡ Yuchun Xu, Junxia Yang, Ling Zhang, Keran Lv, Guoqing Ren, [ID] Shengliang Zhai, Tie Yu [ID] * and Weiqiao Deng [ID] *

A new catalytic approach is pioneered to achieve CO_2 methanation *via* a single atom alloy Ir/Ni catalyst using a ball-milling method. This Ir/Ni catalyst exhibits a TOF_{CH4} of 10244 h^{-1} and a 220 h lifetime at 350 °C without deactivation, illustrating excellent catalytic efficiency in the presence of mechanical energy.

Introduction

A shortage of energy is one of the significant challenges for human society, and exploring new resources or recycling wastes that can be used as substitutes for fossil fuels could yield suitable candidates. CO_2 is one of the greenhouse gases and is released on a massive scale from exhaust gases. It has been widely studied as an energy-generation scaffold with considerable experimentation to produce methane, syngas, formic acid, hydrocarbons, and other valuable chemicals.[1–5] During various conversion routes, CO_2 methanation produces CH_4 directly as an energy resource. If the H_2 could be generated from the photolysis of water, the utilization of green H_2 during the CO_2 methanation reaction presents an unprecedented technological advantage in this specific area.

In 1902, Paul Sabatier and Jean-Baptiste Senderens discovered CO and CO_2 methanation.[6,7] After a century of development, CO_2 methanation mechanistic studies and catalyst R&D have sufficiently advanced so that industrialization of this technology is the next step. There have been many catalysts utilized to increase the CH_4 production efficiency, including noble metal catalysts (Ru, Rh, and Pd)[8–10] and transition metal catalysts (Co, Fe, and Ni).[11–13] There has been intensive research on Ni catalysts due to their low cost and high activity under high temperature.

New concepts

This work achieved the CO_2 methanation reaction through a mechanical catalysis method in a 'gas–gas' system. The mechanical energy induced by the collision between the vessel and the grinding medium (metal balls) was able to activate reactants under mild conditions using a different rationale compared with thermo-catalysis, electro-catalysis, or photo-catalysis methods, with a higher efficiency of the mechanical energy to stimulate methanation. Mechanical catalysis requires the catalyst to integrate with the grinding medium, and therefore we constructed an atomically dispersed Ir–Ni alloy structure on the surface of Ni balls to simultaneously serve as the grinding medium and catalyst. Single-atom Ir significantly increased the catalytic efficiency, and the Ir–Ni alloy structure greatly inhibited noble metal sintering. The collision between the metal balls or/and vessel removed the deposited coke on the metal surface, and therefore mechanical catalysis greatly increased the catalyst lifetime without deactivation as compared with a fixed-bed reactor. An efficiency comparison between mechanical catalysis and thermo-catalysis methods for CO_2 conversion revealed that mechanical energy exhibits the desired catalytic efficiency. This work utilized CO_2 methanation as a 'gas–gas' model reaction to prove the high catalytic efficiency of the mechanical catalysis approach and pioneers a new direction for single-atom metals as catalysts in mechanochemistry fields.

However, Ni catalysts present low CO_2 conversion at low temperatures, while the high reaction temperature during methanation causes catalyst deactivation during metal sintering and carbon deposition, along with low energy efficiency.[14]
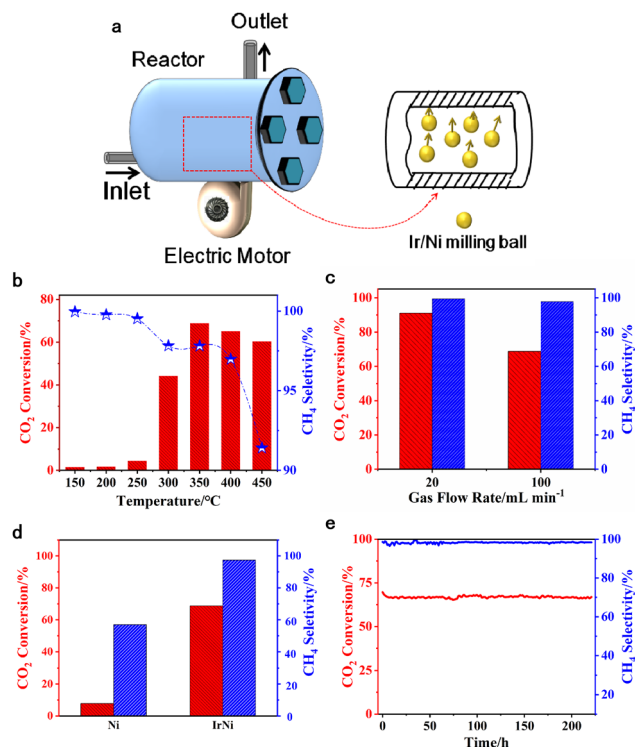
To improve the application potential of Ni-based catalysts, additional metallic elements are normally employed as promoters, and the strong interaction between various metal alloy structures increases the catalytic activity and stability. Previously reported metal promotors include Co, Fe, Ru, Rh, Pt, Pd, and Re in Ni–M bimetallic catalysts.[15] In addition to their promoter action, the catalyst carrier also exhibits a significant effect on CO_2 activation during the methanation process.[13,16–18] Therefore, constructing an alloy structure for an active metal to determine the optimal support for CO_2 adsorption and activation are considered in this study to explore an efficient methanation catalyst.

Except for the catalyst design, this work pioneers a new approach for the mechanical catalysis method to be applied in

Institute of Molecular Sciences and Engineering, Institute of Frontier and Interdisciplinary Science, Shandong University, Qingdao, Shandong, 266237, China. E-mail: dengwq@sdu.edu.cn, yutie043116@tju.edu.cn

† Electronic supplementary information (ESI) available: Experimental details, SEM, TEM, XPS, TG, Electrochemical performance, Computations. See DOI: https://doi.org/10.1039/d3nh00040k

‡ These authors contributed equally to this work.

increasing CO_2 methanation efficiency in the presence of mechanical energy. Mechanical catalysis utilizes mechanical energy from the collision between milling balls and vessel to induce the catalytic reaction, and the collision pattern includes friction, shearing, and collision between two mediums. Mechanocatalysis has been considered as one of the top ten emerging technologies in chemistry, and a previous mechanocatalysis method was utilized to achieve C–N and C–C cross-coupling, cycloaddition, polymer reaction, and C–H activation in previously reported 'solid–solid' systems.[19,20] Recently, the mechanical catalysis method was successfully applied to synthesize ammonia from N_2 and H_2, and the reports noted that the efficiency was greater when mechanical energy was used to activate N_2, with this method greatly moderating the reaction conditions in the batch reaction system.[21,22]

Consequently, we utilized a custom-built vibration reactor (Fig. 1a) to explore mechanical reactions in a continuous gas flow. The active metal species was loaded on metallic milling balls, which simultaneously acted as the catalyst and collision medium. The mechanical energy is produced from the collision between the milling balls and the reactor inner wall, which occurs with a vertical motion. The collision frequency is regulated by the electric motor under the vibration reactor.

Because decreasing the active metal size, especially the atomic dispersion, boosts its catalytic activity,[23–27] iridium (Ir) was impregnated on Ni metal balls to form a single atomic alloy structure in this work. The optimum reaction conditions were firstly investigated to maximize the CH_4 yield, and the Ir distribution and charge were also estimated to understand the bulk structure of the Ir/Ni catalyst. Additionally, the catalytic stability was examined, and a mechanistic study was undertaken to propose a plausible rationale for CO_2 methanation under mechanical catalysis conditions.

Results and discussion

Fig. 1 shows the methanation performance over Ni and Ir/Ni catalysts. Fig. 1b presents the methanation performance from 150–450 °C over the Ir/Ni catalyst, and the desired CO_2 conversion was achieved at 350 °C and began to decrease above 350 °C. Because CO_2 methanation is a thermodynamically unfavorable process, the higher temperature inhibited an increase in CO_2 conversion. Additionally, the CH_4 selectivity in effluent decreased with the increasing reaction temperature due to the formation of CO as byproduct, and the reason for this might be the occurrence of a reverse water–gas reaction at high temperatures ($CO_2 + H_2 = H_2O + CO$).

With respect to CO formation, the chromatograph spectra detected the CO in the product, and it increased from 150 to 450 °C. In addition, increasing the space velocity decreased the CO_2 conversion and the CH_4 selectivity at 350 °C and 800 rpm, as shown in Fig. 1c. The Ir doping significantly increased the CO_2 conversion from 8% to 69%, and the CH_4 selectivity rose from 57% to 98%, as shown in Fig. 1d. It was more intriguing to improve the CH_4 selectivity and inhibit CO generation on Ir/Ni, illustrating the modification of the reaction pathway due to the presence of Ir. Finally, a stability test of CO_2 methanation over Ir/Ni was conducted at 350 °C, 800 rpm, and 100 mL min^{-1} inlets. The CO_2 conversion and CH_4 selectivity were maintained at 64% and 98%, respectively, over 220 h in Fig. 1(e), indicating the superior stability of Ir/Ni for CO_2 methanation.

As a control experiment, an Ir–Ni/Al_2O_3 catalyst (0.5 wt% for Ir loading, and 10 wt% for Ni loading) was also synthesized by an impregnation method, and its lifetime test is shown in Fig. S1 (ESI†). It only presented 34% CO_2 conversion and 99% CH_4 selectivity, while the reactivity continuously decreased with time on stream. Fig. S2 (ESI†) compares some representative catalysts and their methanation performance over the past few decades. The Ir/Ni catalyst exhibited excellent reactivity and stability through the mechanical catalysis method at a moderate temperature range.

Fig. 2 shows the appearance of Ir/Ni and Ir–Ni/Al_2O_3 milling balls. Fresh Ir–Ni/Al_2O_3 presents with a cyan color in Fig. 2c, which turned to black after CO_2 methanation, as shown in Fig. 2d. The color variation was mainly induced by Ni^{2+} reduction and coke during the reaction process, and the 3.5% weight loss above 400 °C from the thermogravimetric (TG) profiles in Fig. S3 (ESI†) proved the coke formation.

Fig. 1 (a) A schematic diagram of the vibration reactor and its vertical work mode. (b) The catalytic activity of Ir/Ni catalysts as a function of reaction temperature. Reaction conditions: 150–450 °C, 800 rpm, and 100 mL min^{-1} flow rate. (c) The methanation performance under different flow rates. Reaction conditions: 350 °C, 800 rpm, and 20–100 mL min^{-1} flow rate. (d) The catalytic activity of Ni and Ir/Ni catalysts. Reaction conditions: 350 °C, 800 rpm, and 100 mL min^{-1} flow rate. (e) Ir/Ni catalysts lifetime study under 350 °C, 800 rpm, and 100 mL min^{-1} flow rate.

Fig. 2 Appearance of (a) fresh and (b) used Ir/Ni. Appearance of (c) fresh and (d) used Ir–Ni/Al$_2$O$_3$ catalysts.

Nevertheless, the Ir/Ni catalysts did not significantly change before or after the reaction (Fig. 2a and b). Also, no coke was detected on the Ir/Ni metal surface, which implied the complete dissociation of CO$_2$ into C atoms or inhibition of other coke-generation reactions over the Ir/Ni catalyst in contrast to metal oxide catalysts.

The scanning electron microscopy (SEM) images in Fig. 3 reveal the morphology of the Ir/Ni metal surface. The fresh Ir/Ni surface was uniform and flat in Fig. 3a and b, but the surface became slightly rough and compact after 220 h of reaction, as shown in Fig. 3c and d. Moreover, many small holes existed on the pristine Ni metal surface that were maintained after calcination and reaction, and they increased the surface defects. The element mapping spectra for the metal surface (Fig. 3e–l) were further used to analyze the metal dispersion. For a fresh Ir/Ni sample, C, O, and Ni were uniformly distributed, and no Ir

signal was recorded (Fig. 3e–h), which was caused by its low loading and a signal that was too weak for adequate dispersion. For the used Ir/Ni sample, the surface atom dispersion did not change after 220 h of reaction (Fig. 3i–l), proving that no metal sintering or aggregation occurred during the reaction process. The surface morphology change might be induced by the preparation process and mechanical collision during the reaction process. In the Supplementary Information, an additional energy dispersive X-ray spectroscopy (EDS) spectrum of the raised particle on the metal surface is shown in Fig. S4 (ESI†), and only Ni, O, and C were recorded. Therefore, there was no relationship between the distortion of the metal surface and the Ir sintering.

The X-ray diffraction (XRD) pattern in Fig. 4a revealed that the Ni metal only presented peaks for the Ni *fcc* structure. After Ir loading, the Ni and NiO phase were detected, and no Ir or IrO$_2$ phases were recorded. The new shoulder peaks appearing over the Ir/Ni sample at 43° were assigned to the Ir–Ni alloy.[28] The partial NiO phase indicated that the annealing treatment during the preparation process was not able to completely reduce the surface metal elements. In addition, the characteristic peaks of the used Ir/Ni catalyst were identical to those of the fresh Ir/Ni catalyst without change, which illustrated the catalytic stability.

X-ray photoelectron spectroscopy (XPS) was used to investigate the valence state of the metallic elements on the metal surface of the Ir/Ni catalyst before and after the reaction. In Fig. 4d, the surface Ni exhibited reduced Ni^0 and oxidative Ni^{2+} states, and their molar ratio (Ni^0/Ni^{2+}) equaled 1 from the peak-fitting results. This was also supported by the NiO phase from the XRD results. The Ir 5f spectra in Fig. 4c only presented reduced Ir^0 species, while the Ir 5f binding energy (61.9 eV) shifted to a higher binding energy direction, implying electron deficiency on Ir atoms.[29] It should be noted that in the O 1s XPS spectra in Fig. S5 (ESI†), the Ni and Ir valence states on the metal surface of the used Ir/Ni catalyst did not change, confirming that the Ir–Ni structure was intact during the methanation reaction. In Fig. 4b, no new carbide species were found from the C 1s spectrum after comparison of the
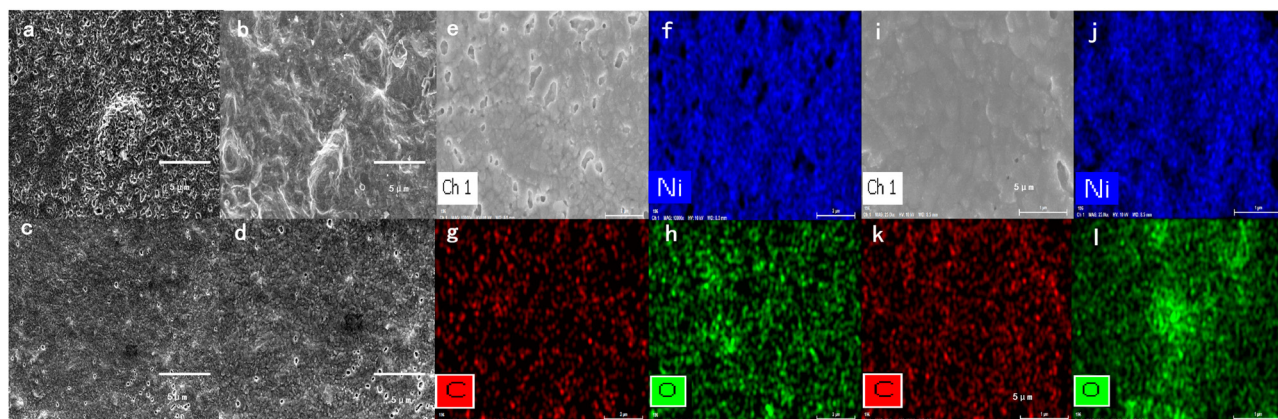

Fig. 3 SEM images of (a and b) fresh and (c and d) used Ir/Ni metal surfaces. Elements mapping spectra of (e)–(h) fresh Ir/Ni and (i)–(l) used Ir/Ni samples.
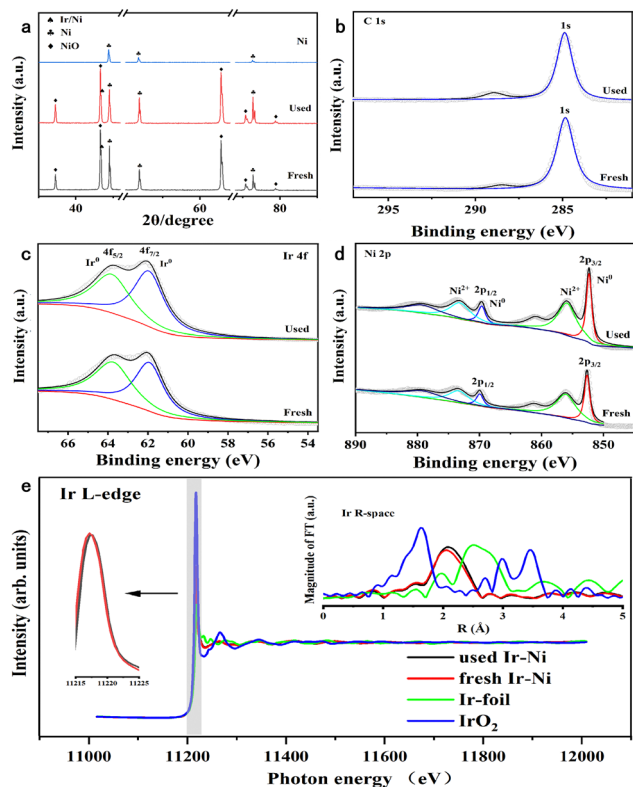
Fig. 4 (a) XRD patterns for Ni and fresh and used Ir/Ni samples. (b–d) Ni 2p, Ir 4f, and C 1s XPS spectra of fresh and used Ir/Ni. (e) XANES spectra of the Ir L_3-edge from the Ir/Ni catalyst, with Ir foil and IrO_2 as references. Inset: Ir L_3-edge EXAFS in R space from the Ir/Ni catalyst, with Ir foil and IrO_2 as references.

fresh and used Ir/Ni samples, which was consistent with the above result demonstrating no coke generation on the Ir/Ni catalyst.

The X-ray absorption near-edge spectroscopy (XANES) and extended X-ray absorption fine structure (EXAFS) were measured to examine the coordination structure of Ir species on the Ir/Ni catalyst, as shown in Fig. 4e. The intensity of the white line represents the charge of the Ir species, and the increasing intensity denotes the charge increase. The white line intensity for the Ir/Ni catalyst was between that of Ir foil and IrO_2, but similar to that of Ir foil, which illustrates that the Ir charge was near 0, but presented an electron-deficient state.

The Fourier transform spectra of EXAFS in R-space exhibited a primary peak at 2.12 Å, which was assigned to the Ir–Ni alloy structure because this coordination path was clearly different with Ir–Ir from Ir foil or Ir–O from IrO_2. Additionally, the EXAFS spectra also proved that there was no existence of Ir particles over the Ir/Ni metal surface. The profile fitting results in R-space demonstrated that the Ir coordination number was 6 for the Ir–Ni band in Table S1 (ESI†), which further proved the formation of atomically dispersed Ir species on the Ni surface. Compared with the fresh Ir/Ni catalyst, the used Ir/Ni sample presented the identical Ir XANES spectra, and their profiles almost overlapped. The Ir–Ni coordination path in the FT EXAFS spectra was the same, implying that the Ir–Ni structure was intact during the CO_2 methanation reaction.
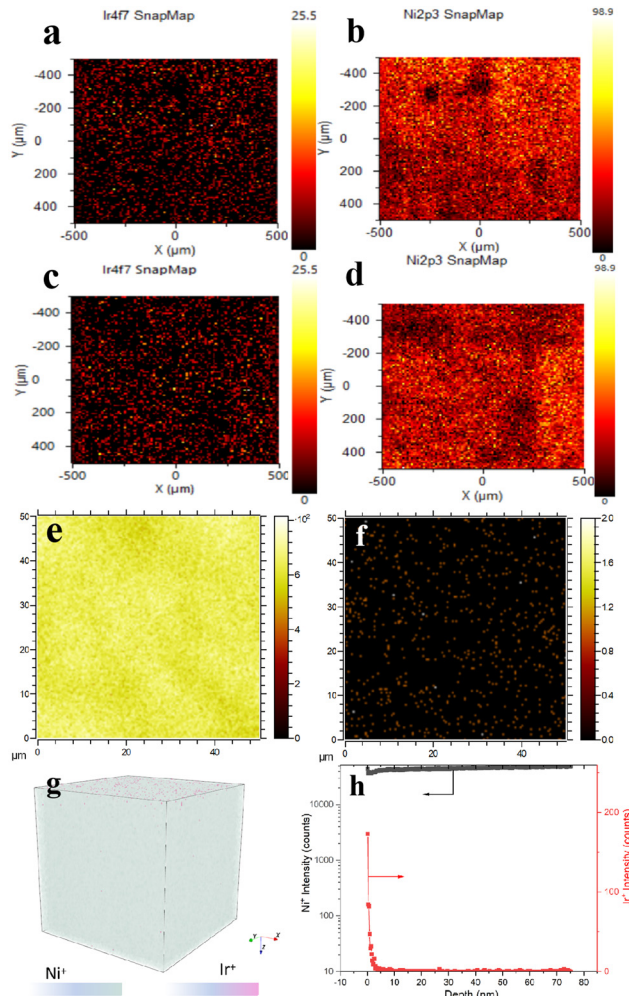

Fig. 5 Surface element mapping images from XPS spectra over fresh Ir/Ni and used Ir/Ni catalyst. The spot size was controlled at 10 μm, and the scanning times were 20 for each spot. (a) Ir and (b) Ni mapping spectra over a fresh Ir/Ni sample. (c) Ir and (d) Ni mapping spectra over a used Ir/Ni sample. Abundance maps of (e) Ni^+ and (f) Ir^+ over a 50 × 50 μm² field of view from the Ir/Ni surface region. (g) A 3D TOF-SIMS map of the Ir signal on the Ni substrate. (h) The Ni^+ and Ir^+ signals obtained by TOF-SIMS analysis with respect to the diffusion depth.

Because the Ir/Ni milling ball in this work is in a pure metallic phase and too thick, the XPS element mapping spectra in Fig. 5 presented its advantages in examining the surface atom dispersion. The element mapping spectra in Fig. 5a demonstrated that the doped Ir atoms were well dispersed on the Ni metal surface, and no Ir particles were detected in the scanning area. The mapping spectra for the used Ir/Ni catalyst shown in Fig. 5c and d presented identical results, consisting of well-dispersed Ir species and a Ni substrate that illustrated no detected change in the Ir/Ni structure during the CO_2 methanation process.

Time-of-flight secondary ion mass spectrometry (TOF-SIMS) is a sensitive surface analytical technique that can be adequately used to reflect Ir spatial localization on the Ni substrate. Fig. 5e–h revealed that Ir was well dispersed on the surface of the Ni substrate without aggregation, and the distribution

depth of Ir from 0–3 nm was induced by the rough geometry of the Ni surface, as shown in Fig. S6 (ESI†). The spent Ir/Ni sample presented an Ir dispersion that was identical to that of the fresh Ir/Ni sample in Fig. S7 (ESI†), which proved the intact Ir/Ni structure. Fig. 4 combines the XRD and XANES results for Ir distribution, and it was identified that only atomically dispersed Ir species were formed on the Ir/Ni catalyst.

Fig. 6 presents the CO_2 + H_2 diffuse reflectance infrared Fourier transform spectroscopy (DRIFTS) results over the Ni and Ir/Ni catalysts. Prior to this test, the CO_2 adsorption behavior over those two samples was estimated using DRIFTS, as shown

in Fig. S8a and b (ESI†). Characteristic peaks after CO_2 adsorption appeared in three regions: 1300–1800 cm^{-1}, 2200–2400 cm^{-1}, and 3500–3800 cm^{-1}, which were ascribed to carbonate/formate-like species,[30–32] gaseous absorbed CO_2 species, and hydrogen carbonates/hydroxyls, respectively.[31,33] Notably, the identical DRIFTS results for CO_2 adsorption in Fig. S8a and b (ESI†) over two samples demonstrated that the doped Ir species exhibited inferior CO_2 adsorption ability, and Ni was the main CO_2 adsorption site. Nevertheless, when CO_2 + H_2 was introduced onto the catalysts, the Ir/Ni catalyst presented many more carbonates and formate species than the Ni catalyst, as shown in Fig. 6, and the corresponding peak intensities greatly strengthened. (The remainder of the DRIFTS results is shown in Fig. S8c and d, ESI.†)

Specifically, the peaks at 1130, 1361, and 1735 cm^{-1} in Fig. 6a were assigned to formate species, and the peak at 1530 cm^{-1} belongs to the O–C–O asymmetric vibration in formate species.[30,31] The peaks at 1653 and 1434 cm^{-1} were ascribed to carbonate species.[32] It has been documented that monodenate carbonates are easily hydrogenated into formate species during the CO_2 methanation process, and therefore, additional formate species were recorded on the Ir/Ni catalyst as compared to carbonate species. In addition, no adsorbed CO species were detected at 1900–2000 cm^{-1} in Fig. 6, which indicates that the CO route was not the dominant reaction pathway for CH_4 generation and explained the lower CO selectivity in this work. It was concluded that formate species were the main intermediates for CO_2 methanation over the Ir/Ni catalyst, and Ir–Ni possessed much higher reactivity than Ni for CO_2 activation and its subsequent hydrogenation process.

To boost the impact of mechanical energy on the CO_2 methanation reaction, kinetic experiments under static mode and vibration mode (800 rpm) were performed, and are shown in Fig. 6c. The Ir/Ni catalyst under the mechanical catalysis method exhibited higher reaction rates as compared to the thermo-catalysis method. The lower apparent activation energy of mechanical catalysis implied that the addition of mechanical energy introduced variation into the methanation rationale and enhanced the CO_2 conversion efficiency.

The heating effect induced by the mechanical collision between milling balls and vessel is examined in Fig. S9 (ESI†). The slight temperature change demonstrated that the heating effect was not the main mechanical energy transformation pattern. Additionally, the collisional electric charge on the Ir/Ni and Ni balls after collision with steel plates in Fig. S10 and S11 (ESI†) revealed that the doped Ir species greatly increased the electric charge on the Ir/Ni balls as compared with Ni balls, which probably boosted CO_2 activation and energy transformation from mechanical collision into reactant conversion.

The energy consumption under static mode and vibration mode (800 rpm) was also measured by an electricity meter. Under 350 °C, CO_2 methanation under vibration mode and static mode consumed 0.137 kW h and 0.140 kW h energy, respectively. The additional energy consumption from the mechanical vibration was 1.4%, while the obvious improvement in the CO_2 conversion rates as shown in Fig. 6c proved the high catalytic efficiency of mechanical energy during this reaction
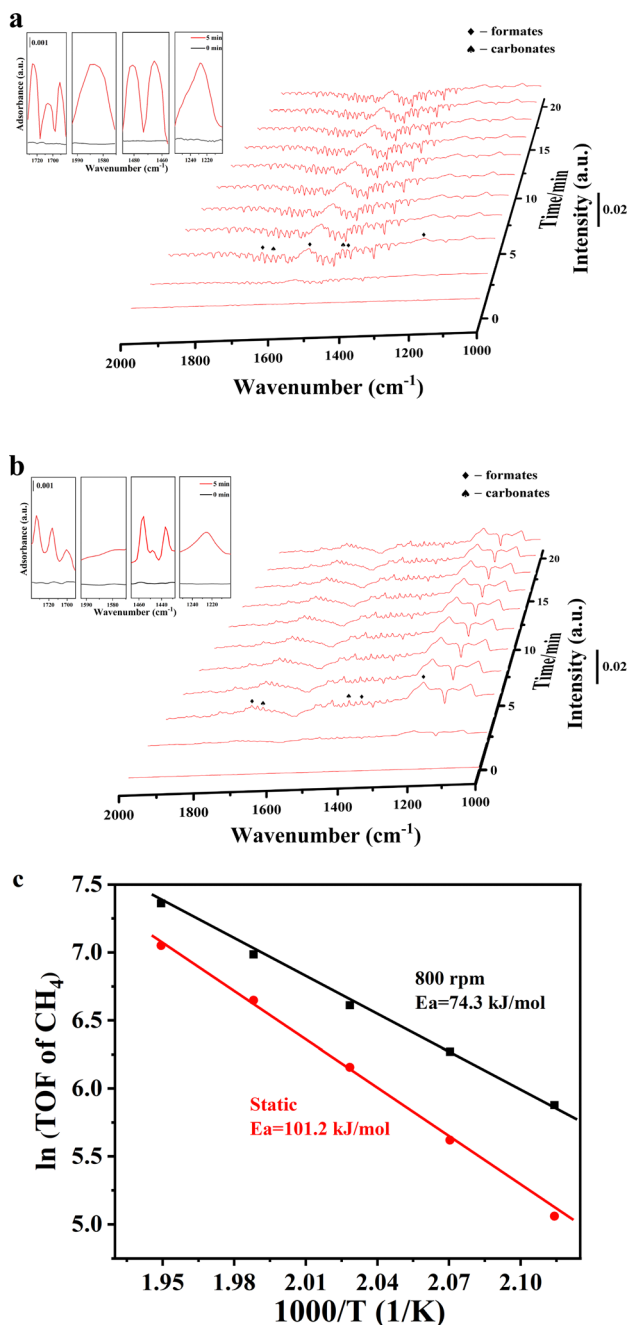
Fig. 6 *In situ* DRIFTS studies of CO_2 + H_2 over (a) Ir/Ni and (b) Ni catalysts under 150 °C. (c) The apparent activation energy from a kinetic activity test.

process. Further studies on mechanistic research and energy transformation patterns would greatly promote the application of this technology for catalytic conversion between energy molecules.

Conclusions

The Ir/Ni single atom alloy catalyst was prepared by an impregnation method and utilized for CO_2 methanation through a mechanical catalysis method. The reaction activity showed that the Ir/Ni catalyst exhibited a superior CO_2 conversion rate and state-of-the-art reaction stability. The bulk characterization results proved that Ir was atomically dispersed and coordinated with surface Ni atoms in the form of an Ir–Ni alloy, and reduced Ir^0 species presented an electron-efficient state. The Ni atoms on the metal surface possessed reduced Ni^0 and oxidative Ni^{2+} states at the same time. The Ni sites were the main CO_2 adsorption sites, and an Ir–Ni alloy was the reaction site for H_2 activation and the subsequent hydrogenation reaction. After 220 h of reaction, the Ir/Ni catalyst exhibited identical surface atom distribution and valence states, and the stable Ir–Ni alloy structure enabled its long lifetime. Compared with the oxide-supported Ir–Ni/Al_2O_3 catalyst, the Ir/Ni catalyst exhibited excellent coke-resistant performance, and the mechanochemical catalysis method effectively boosted the reaction efficiency with the addition of mechanical energy.

Author contributions

T. R. and Z. Y. J. designed the experiments, analyzed the data, and wrote the manuscript. Y. J. X. and X. Y. C conducted the XRD, XPS, and XANES analyses. Z. L. and Z. S. L. performed the DRIFTS experiments. L. K. R. integrated the studies, and reviewed and edited the manuscript. Y. T. conceived the idea, planned and directed the studies, and wrote the manuscript. D. W. Q. oversaw the project. All authors confirmed the data in the manuscript.

Conflicts of interest

The authors declare no conflicts of interest.

Acknowledgements

Notes and references

1 A. I. Osman, M. Hefny, M. I. A. Abdel Maksoud, A. M. Elgarahy and D. W. Rooney, *Environ. Chem. Lett.*, 2021, **19**, 797–849.

2 J. Long, S. Chen, Y. Zhang, C. Guo, X. Fu, D. Deng and J. Xiao, *Angew. Chem., Int. Ed.*, 2020, **59**, 9711–9718.

3 T. A. Atsbha, T. Yoon, P. Seongho and C. J. Lee, *J. CO2 Util.*, 2021, **44**, 101413–101434.

4 W. Wang, S. Wang, X. Ma and J. Gong, *Chem. Soc. Rev.*, 2011, **40**, 3703–3727.

5 G. Tian, C. Zhang and F. Wei, *Nanoscale Horiz.*, 2022, **7**, 1478–1487.

6 S. Roensch, J. Schneider, S. Matthischke, M. Schlueter, M. Goetz, J. Lefebvre, P. Prabhakaran and S. Bajohr, *Fuel*, 2016, **166**, 276–296.

7 M. Thema, F. Bauer and M. Sterner, *Renewable Sustainable Energy Rev.*, 2019, **112**, 775–787.

8 A. Beuls, C. Swalus, M. Jacquemin, G. Heyen, A. Karelovic and P. Ruiz, *Appl. Catal., B*, 2012, **113–114**, 2–10.

9 G. Garbarino, D. Bellotti, P. Riani, L. Magistri and G. Busca, *Int. J. Hydrogen Energy*, 2015, **40**, 9171–9182.

10 C. Yan, C. H. Wang, M. Lin, D. Bhalothia, S. S. Yang, G. J. Fan, J. L. Wang, T. S. Chan, Y. L. Wang, X. Tu, S. Dai, K. W. Wang, J. H. He and T. Y. Chen, *J. Mater. Chem. A*, 2020, **8**, 12744.

11 H. Kierzkowska-Pawlak, J. Tyczkowski, J. Balcerzak and P. Tracz, *Catal. Today*, 2019, **337**, 162–170.

12 J. Kirchner, C. Zambrzycki, S. Kureti and R. Güttel, *Chem. Ing. Tech.*, 2020, **92**, 603–607.

13 K. Ray and G. Deo, *Appl. Catal., B*, 2017, **218**, 525–537.

14 S. Rönsch, J. Schneider, S. Matthischke, M. Schlüter, M. Götz, J. Lefebvre, P. Prabhakaran and S. Bajohr, *Fuel*, 2016, **166**, 276–296.

15 A. I. Tsiotsias, N. D. Charisiou, I. V. Yentekakis and M. A. Goula, *Nanomaterials*, 2021, **11**, 28.

16 P. Panagiotopoulou, *Appl. Catal., A*, 2017, **542**, 63–70.

17 X. Jia, X. Zhang, N. Rui, X. Hu and C. J. Liu, *Appl. Catal., B*, 2019, **244**, 159–169.

18 S. Renda, A. Ricca and V. Palma, *Int. J. Hydrogen Energy*, 2021, **46**, 12117–12127.

19 S. Hwang, S. Graetz and L. Borchardt, *Chem. Commun.*, 2022, **58**, 1661–1671.

20 F. R. Fan, S. Xie, G. W. Wang and Z. Q. Tian, *Sci. China: Chem.*, 2021, **64**, 1609–1613.

21 G. F. Han, F. Li, Z. W. Chen, C. Coppex, S. J. Kim, H. J. Noh, Z. Fu, Y. Lu, C. V. Singh, S. Siahrostami, Q. Jiang and J. B. Baek, *Nat. Nanotechnol.*, 2021, **16**, 325–330.

22 S. Reichle, M. Felderhoff and F. Schüth, *Angew. Chem., Int. Ed.*, 2021, **60**, 26385–26389.

23 Z. Zhang, C. Shen, K. Sun, X. Jia, J. Ye and C. J. Liu, *Mater. Chem. A*, 2022, **10**, 5792–5812.

24 B. Chang, S. Wu, Y. Wang, T. Sun and Z. Cheng, *Nanoscale Horiz.*, 2022, **7**, 1340–1387.

25 Z. Kou, W. Zang, P. Wang, X. Li and J. Wang, *Nanoscale Horiz.*, 2020, **5**, 757–764.

26 R. T. Hannagan, G. Giannakakis, R. Reocreux, J. Schumann, J. Finzel, Y. C. Wang, A. Michaelides, P. Deshlahra, P. Christopher, M. Flytzani-Stephanopoulos, M. Stamatakis and E. C. H. Sykes, *Science*, 2021, **372**, 1444.

27 G. Kyriakou, M. B. Boucher, A. D. Jewell, E. A. Lewis, T. J. Lawton, A. E. Baber, H. L. Tierney, M. Flytzani-Stephanopoulos and E. C. H. Sykes, *Science*, 2012, **335**, 1209.

28 K. Sasaki, K. A. Kuttiyiel, L. Barrio, D. Su, A. I. Frenkel, N. Marinkovic, D. Mahajan and R. R. Adzic, *J. Phys. Chem. C*, 2011, **115**, 9894–9902.

29 J. Park, S. Choi, A. Oh, H. Jin, J. Joo, H. Baik and K. Lee, *Nanoscale Horiz.*, 2019, **4**, 727–734.

30 Y. H. Lee, J. Y. Ahn, D. D. Nguyen, S. W. Chang, S. S. Kim and S. M. Lee, *RSC Adv.*, 2021, **11**, 17648–17657.

31 Q. Pan, J. Peng, S. Wang and S. Wang, *Catal. Sci. Technol.*, 2014, **4**, 502–509.

32 Q. Pan, J. Peng, T. Sun, S. Wang and S. Wang, *Catal. Commun.*, 2014, **45**, 74–78.

33 P. A. U. Aldana, F. Ocampo, K. Kobl, B. Louis, F. Thibault-Starzyk, M. Daturi, P. Bazin, S. Thomas and A. C. Roger, *Catal. Today*, 2013, **215**, 201–207.